JfM RAPIDS

A framework for assessing the Reynolds analogy in turbulent forced convection over rough walls

Francesco Secchi[1] , **Davide Gatti**[1] , **Ugo Piomelli**[2] and **Bettina Frohnapfel**[1]

[1]Institute of Fluid Mechanics, Karlsruhe Institute of Technology, Kaiserstraße 10, 76131 Karlsruhe, Germany

[2]Department of Mechanical and Materials Engineering, Smith Engineering, Queen's University, Kingston, ON, K7L 3N6, Canada

Corresponding author: Francesco Secchi, francesco.secchi@kit.edu

This study introduces a novel approach to investigate the Reynolds analogy in complex flow scenarios. It is shown that the total mechanical energy B, *viz.* the sum of kinetic energy and pressure work, and the field $\Gamma = \theta^2/2$ (where θ is the transported passive scalar) are governed by two equations that are similar in form, when time-averaged for statistically stationary flows. For fully developed channel flows the integral energy balance links the mean bulk velocity and scalar with the volume averages of the respective dissipation rates, allowing the assessment of the Reynolds analogy in terms of the dissipation fields. This approach is tested on direct numerical simulation data of rough-wall turbulent channel flow at two different roughness Reynolds numbers, namely $k^+ = 15$ and $k^+ = 90$. For a unit Prandtl number, the same qualitative behaviour is observed for the mean wall-normal distributions of the budget-equation terms of B and Γ, the latter being larger than the corresponding terms in the mechanical-energy budget. The Reynolds decomposition of the flow into temporal mean and stochastic parts reveals that roughness primarily affects the mean-flow dissipation. For the $k^+ = 90$ case, the analysis shows that attached-flow and high-shear regions dominate the integral mean scalar and momentum transfer and exhibit the greatest differences between the mean mechanical and scalar dissipation rates. In contrast, well-mixed regions, sheltered by large roughness elements, contribute similarly and minimally to the integral scalar and momentum transfer.

Key words: turbulent convection, turbulence simulation

F. Secchi, D. Gatti, U. Piomelli and B. Frohnapfel

1. Introduction

As fluids flow over solid walls, the transfer of internal energy and momentum across the fluid–solid interface is expected to be similar, assuming identical boundary conditions and driving sources (e.g. pressure gradient and heat source) and comparable molecular momentum and thermal diffusivities. This similarity is known as the Reynolds analogy, named after Reynolds' pioneering observations on pipe-flow heat transfer (Reynolds 1874). Although the ideal conditions for this analogy are rare in practical applications, understanding its breakdown in simplified scenarios can improve predictive heat-transfer models and flow-control strategies, particularly when aiming for dissimilar control of momentum and heat transfer (Hasegawa & Kasagi 2011). This work focuses on cases where temperature differences are small enough that buoyancy effects are negligible, allowing temperature to be treated as a passive scalar field. Thus, temperature and scalar field will be used interchangeably.

An analogy between momentum and heat transfer might suggest a direct similarity between the velocity and temperature fields. However, this comparison is formally inappropriate due to their different nature: velocity is a three-dimensional solenoidal vector field, while temperature is a scalar field. As pointed out by Abe, Antonia & Kawamura (2009), a more sound approach consists in seeking similarity between the turbulent kinetic energy $\overline{\kappa} = \overline{u'_i u'_i}/2$, where u_i denotes the ith velocity component, and the scalar-fluctuation variance $\overline{\gamma} = \overline{\theta'^2}/2$ (a prime superscript indicates temporal fluctuations, whereas an over-bar stands for time averaging). These two quantities, both scalar fields governed by similar equations (Corrsin 1952), are good candidates to assess momentum and scalar similarities within the flow field.

Their qualitative similarity is well-established for flows that closely adhere to the Reynolds analogy, such as smooth-wall turbulent channel flows (Kim & Moin 1989; Kasagi, Tomita & Kuroda 1992; Antonia, Abe & Kawamura 2009; Pirozzoli, Bernardini & Orlandi 2016). In contrast, departures from analogy can manifest themselves through dissimilar distributions of velocity and scalar fluctuations. For instance, for turbulent flows over surface roughness, Leonardi *et al.* (2015); Peeters & Sandham (2019); and Hantsis & Piomelli (2022) have shown that roughness acts differently on the momentum and scalar turbulent fluxes, thereby modifying the production of velocity and scalar fluctuations within the roughness sublayer.

Although departures from the analogy can be observed through differing distributions of $\overline{\kappa}$ and $\overline{\gamma}$, linking this observation to a quantitative measure of the Reynolds analogy remains challenging. In wall-bounded flows, the analogy is measured by the Reynolds-analogy factor $RA = 2C_h/C_f$, with $RA = 1$ indicating perfectly similar momentum and scalar transfer (here C_f and C_h are the friction coefficient and Stanton number, respectively). Given that the total momentum and scalar fluxes at the wall, and thus C_f and C_h, must be related to the total power input required to sustain the flow, inclusive of mean and turbulent contributions, it seems short-sighted to seek a direct connection between C_f and C_h and turbulent energy fields (e.g. $\overline{\kappa}$ and $\overline{\gamma}$).

Based on this argument, we propose to consider the Reynolds-analogy problem in terms of the total mechanical energy and half of the squared scalar field, $K = u_i u_i/2$ and $\Gamma = \theta^2/2$, respectively. Their governing equations can be written in the form

$$\frac{\partial K}{\partial t} + u_i \frac{\partial B}{\partial x_i} = \nu \frac{\partial^2 B}{\partial x_i \partial x_i} - \nu \omega_i \omega_i + f_i u_i, \qquad (1.1a)$$

$$\frac{\partial \Gamma}{\partial t} + u_i \frac{\partial \Gamma}{\partial x_i} = \alpha \frac{\partial^2 \Gamma}{\partial x_i \partial x_i} - \alpha \frac{\partial \theta}{\partial x_i} \frac{\partial \theta}{\partial x_i} + q\theta, \qquad (1.1b)$$

where $B = K + (p/\rho)$ is the total mechanical energy, p, ρ, ν, and α are, respectively, the pressure, fluid density, kinematic viscosity and thermal diffusivity, ω_i is the ith vorticity component, and f_i and q are, respectively, external volume-force and scalar-source terms. Equation (1.1a) is obtained by taking the inner product of the velocity with the momentum equation, and recalling that $p_{,ii}/\rho = \omega_i \omega_i/2 - s_{ij} s_{ij}$ (Bradshaw & Koh 1981). The notation $(\cdot)_{,i}$ indicates differentiation in the i direction. Here $s_{ij} = (1/2)(u_{i,j} + u_{j,i})$ is the strain-rate tensor. Similarly, (1.1b) is obtained by multiplying the transport equation for θ by θ itself.

Equations (1.1a) and (1.1b) highlight a key difference in the evolution of K and Γ: the point-wise time rate of change of K depends on the transport and molecular diffusion of total mechanical energy B, while that of Γ depends solely on the transport and diffusion of Γ itself. For statistically stationary flows, time averaging the equations yields two steady-state advection–diffusion equations for $\overline{B}$ and $\overline{\Gamma}$, in which the terms $\nu \overline{\omega_i \omega_i}$ and $\alpha \overline{\theta_{,i} \theta_{,i}}$ play the role of dissipation rates of $\overline{B}$ and $\overline{\Gamma}$, respectively. Note that, according to (1.1a), the former occurs through the action of the local dissipation rate of kinetic energy, $\nu \omega_i \omega_i$ (Wu, Zhou & Fan 1999). For statistically stationary flows, $\nu \overline{\omega_i \omega_i}$ amounts also to the local dissipation rate of the time-averaged total mechanical energy, $\overline{B}$; this equivalence holds because the balance of $\overline{B}$ differs from that of $\overline{K}$ only through the pressure transport terms of convection and molecular diffusion. The integral form of (1.1a) and (1.1b) establishes a link between the total power necessary to sustain the flow and field quantities associated with the mechanical and scalar energy. This connection can be further extended to include the total momentum and scalar fluxes at the wall, thus determining a bridge to the Reynolds-analogy factor.

This work explores this approach to study fully developed turbulent channel flow over homogeneous random surface roughness. Surface roughness impacts scalar and momentum transfer depending on the relative size of roughness elements to the viscous sublayer thickness imposed by the flow. In the hydraulically smooth regime, where roughness elements are significantly smaller than the viscous sublayer thickness, no roughness effects are observed. Heat and momentum transfer occur primarily via molecular diffusion across the channel walls, maintaining similar transfer mechanisms. As the roughness size approaches that of the viscous sublayer, the flow enters the transitionally rough regime. Here, the momentum transfer departs from an analogous behaviour due to the momentum loss caused by the form-drag induced by roughness elements, which lacks an equivalent mechanism for the heat transfer. Ultimately, in the fully rough regime, the form-drag becomes the predominant contribution to momentum loss, whereas there is not yet unanimous consensus on a scalar transfer law in this regime (see e.g. the recent review of Hantsis & Piomelli 2024).

In the present work, direct numerical simulations (DNS) are used to replicate two selected cases presented by Thakkar, Busse & Sandham (2017); Thakkar (2017); Thakkar, Busse & Sandham (2018) and Peeters & Sandham (2019). In this context, (1.1a) and (1.1b) provide a novel perspective on the breaking of the Reynolds analogy, enabling both qualitative and quantitative assessments of the phenomenon.

This work is organized as follows: in § 2, (1.1a) and (1.1b) are specialized for the flow under investigation; the details about the simulation set-ups and the numerical procedure are presented in § 3; results are reported in § 4, while concluding remarks are summarized in § 5.

2. Problem formulation

We consider a fully developed turbulent channel flow with mean streamwise velocity directed along the $x = x_1$ direction. The wall-normal direction is denoted by $z = x_3$. No-slip and non-penetration boundary conditions are applied at the stationary walls of the channel, where the passive scalar θ is fixed to a constant value θ_w. To have analogous wall boundary conditions for the velocity and the passive scalar field, we set $\theta_w = 0$. Upon non-dimensionalization using viscous units, the time-averaged equations (1.1a) and (1.1b) become

$$\overline{u_i^+ \frac{\partial B^+}{\partial x_i^+}} = \frac{\partial^2 \overline{B}^+}{\partial x_i^+ \partial x_i^+} - \overline{\omega_i^+ \omega_i^+} + \frac{1}{Re_\tau}\delta_{1i}\overline{u_i}^+, \tag{2.1a}$$

$$\frac{1}{Pr}\overline{u_i^+ \frac{\partial \Gamma^+}{\partial x_i^+}} = \frac{1}{Pr^2}\frac{\partial^2 \overline{\Gamma}^+}{\partial x_i^+ \partial x_i^+} - \frac{1}{Pr^2}\overline{\frac{\partial \theta^+}{\partial x_i^+}\frac{\partial \theta^+}{\partial x_i^+}} + \frac{1}{Pe_\tau}\overline{\theta}^+, \tag{2.1b}$$

where $Re_\tau = u_\tau\delta/\nu$, $Pe_\tau = Pr\,Re_\tau$. The friction velocity is $u_\tau = (\tau_w/\rho)^{1/2}$, τ_w being the mean total wall-shear stress and δ the half-channel height. Note that the Prandtl number, $Pr = \nu/\alpha$, can be replaced by the Schmidt number in case θ represented a species-concentration field. The friction passive scalar is defined as $\theta_\tau = \alpha q_w/u_\tau$, where q_w is the mean scalar-flux at the wall, $q_w = (1/A)\int_{A_w} \theta_{,i}\,n_i\,\mathrm{d}A$ (where A_w and A are, respectively, the wetted and plan area of the channel wall, and n_i indicates the unit vector normal to the wall surface). The $+$ superscript is used to denote quantities non-dimensionalised using $\delta_\nu = \nu/u_\tau$, u_τ and θ_τ.

The mean bulk velocity U_b^+ and scalar Θ_b^+ can be computed by integrating, respectively, (2.1a) and (2.1b) over the channel volume $\mathcal{V}$ and dividing the result by the channel volume. Namely,

$$U_b^+ = \frac{Re_\tau}{\mathcal{V}^+}\int_{\mathcal{V}^+}\overline{\omega_i^+ \omega_i^+}\,\mathrm{d}\mathcal{V}^+, \tag{2.2a}$$

$$\Theta_b^+ = \frac{Pe_\tau}{Pr^2\mathcal{V}^+}\int_{\mathcal{V}^+}\overline{\frac{\partial \theta^+}{\partial x_i^+}\frac{\partial \theta^+}{\partial x_i^+}}\,d\mathcal{V}^+. \tag{2.2b}$$

Equation (2.2a) states the integral balance between the total mechanical power exerted by the flow, i.e. U_b^+, and the integral dissipation of mechanical energy on the right-hand side of the equation. Analogously, (2.2b) is interpreted as the integral balance between the mean bulk scalar, Θ_b^+, and the integral dissipation of $\overline{\Gamma}$. Note that these expressions are equivalent to the integral energy and scalar balances presented, for smooth-wall flows, by Laadhari (2007); Abe & Antonia (2016, 2017); Wei (2018). Yet, (2.2a) and (2.2b) remain valid even in the case of non-smooth-wall flows and regardless of the decomposition into mean and turbulent flow contributions.

Expressions (2.2a) and (2.2b) can be inserted in the definitions of the friction coefficient $C_f = 2/U_b^{+2}$ and of the Stanton number $C_h = 1/(U_b^+\Theta_b^+)$, which, in turn, can be used to compute the Reynolds-analogy factor $RA = 2C_h/C_f$:

$$RA = \frac{U_b^+}{\Theta_b^+} = Pr\left(\int_{\mathcal{V}^+}\overline{\omega_i^+ \omega_i^+}\,d\mathcal{V}^+\right) \times \left(\int_{\mathcal{V}^+}\overline{\frac{\partial \theta^+}{\partial x_i^+}\frac{\partial \theta^+}{\partial x_i^+}}\,d\mathcal{V}^+\right)^{-1}. \tag{2.3}$$

This expression relates the Reynolds-analogy factor to quantities defined within the bulk of the flow and, as such, can be instrumental in unveiling flow phenomena that lead to breaking the analogy. It must be emphasized that, locally, departures from the Reynolds
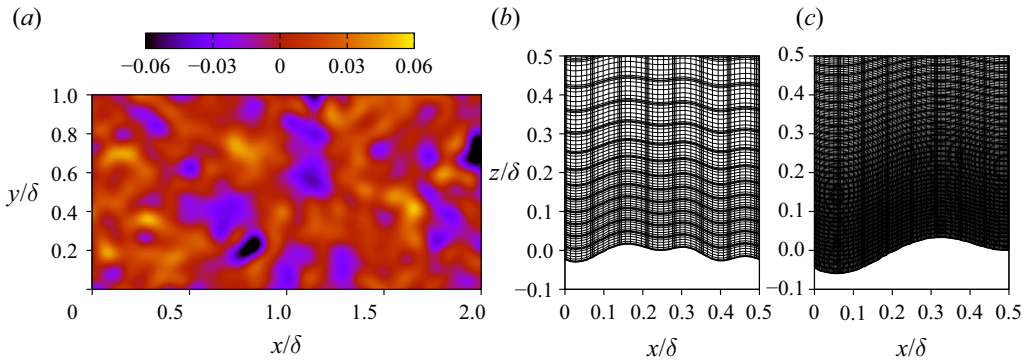
Figure 1. Sample of the roughness topography for the case $k^+ = 15$ (*a*). Details of the computational grid: $k^+ = 15$ case (*b*); $k^+ = 90$ case (*c*).

analysis can manifest themselves through dissimilar distributions of all the terms in (2.1*a*) and (2.1*b*); however, from an intergal perspective, (2.3) shows that a dissimilar scalar and momentum transfer can be quantified globally through the volume integrals of the dissipation rates of $\overline{B}$ and $\overline{\Gamma}$.

3. Case set-ups and numerical procedure

The present numerical simulations replicate two cases of the rough-wall fully developed turbulent channel-flow simulations presented by Thakkar *et al.* (2017), Thakkar (2017), Thakkar *et al.* (2018) and Peeters & Sandham (2019). In particular, in one case the flow is transitionally rough, but close to smooth-wall conditions, with $k^+ = 15$ (here $k^+ = k u_\tau / \nu$, and k is the mean peak-to-trough height of the roughness topography), whereas for the second case, the flow is close to fully rough conditions, with $k^+ = 90$. The roughness topography is obtained from a scan of a real grit-blasted surface and is statistically homogeneous in the wall-parallel directions $x_1 = x$ and $x_2 = y$. A sample of the roughness topography is shown in figure 1. The physical size of the roughness is $k = \delta/12$, for the $k^+ = 15$ case, and $k = \delta/6$, for the $k^+ = 90$ case. The friction Reynolds number is $Re_\tau = 180$ for the former case and $Re_\tau = 540$ for the latter. An additional smooth-wall channel flow at $Re_\tau = 180$ is also simulated. For all the cases, a unit Prandtl number is considered.

The numerical integration of the incompressible Navier–Stokes equations is carried out using the flow solver Nek5000 (Fisher, Lottes & Kerkemeier 2019), which is based on the spectral-element method proposed by Patera (1984). Surface roughness is introduced into the simulations using a body-fitted mesh, obtained by deforming, in the wall-normal direction z, the spectral elements of a plane-channel box having the bottom and top walls at, respectively, $z = 0$ and $z = 2\delta$. The mesh deformation is symmetric with respect to the channel centre line and varies linearly with the wall-normal distance from the bottom wall of the non-deformed channel. As a result, the mean height of the deformed channel is 2δ. Figures 1(*b*) and 1(*c*) illustrate the details of the body-conforming computational meshes used in the two rough-wall cases.

The non-deformed computational domain has size $L_x \times L_y \times 2\delta$ in the streamwise, spanwise and wall-normal directions, respectively. Correspondingly, the number of elements in the three coordinate directions are denoted by n_x, n_y and n_z. A uniform distribution of elements is used in the streamwise and spanwise directions, whereas, in the wall-normal direction, elements are clustered near the channel walls. The domain size, the number of elements in each direction, the polynomial degree of the solution,

k^+	Re_τ	k/δ	L_x/δ	L_y/δ	n_x	n_y	n_z	P	DOF	$T_{avg}U_b/\delta$	U_b^+	Θ_b^+	RA
0	180	0	4π	2π	40	20	36	9th	29×10^6	1875.6	15.63	15.59	1.00
15	180	1/12	5.63	2.815	80	40	36	7th	59×10^6	1042.7	13.72	14.44	0.95
90	540	1/6	5.63	2.815	90	45	108	7th	224×10^6	140.9	10.84	13.62	0.80

Table 1. Simulation parameters. Here, P is the polynomial degree of the solution, whereas DOF indicates the total number of degrees of freedom.
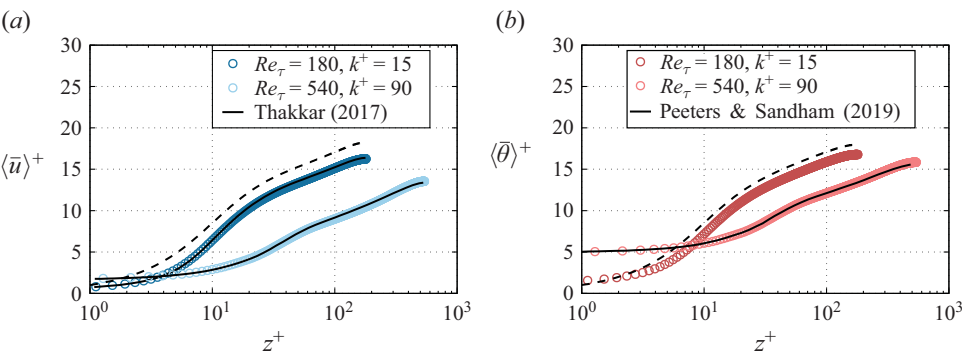

Figure 2. Comparison with data from Thakkar (2017) and Peeters & Sandham (2019). (*a*) Mean streamwise-velocity profiles; (*b*) mean scalar profiles. Black dashed lines indicate smooth-wall data at $Re_\tau = 180$.

and the total number of degrees of freedom (DOF) are reported in table 1. The total number of DOF corresponds to the number of grid points in the physical space and is given by $n_x \times n_y \times n_z \times (P+1)^3$, since each element is divided into $P+1$ grid points. The points distribution along each element direction is non-uniform and follows the Gauss–Legendre–Lobatto distribution of quadrature nodes. This can be appreciated in the panels (*b*) and (*c*) of figure 1 for the case $P = 7$.

The present numerical set-up is validated against the reference data of Thakkar (2017) and Peeters & Sandham (2019). As an example, figure 2 shows a comparison of the mean streamwise-velocity and temperature profiles with the available reference data. In the figure and throughout the text, angular brackets denote intrinsic averaging, i.e. spatial averaging along the homogeneous channel directions performed in fluid regions only; namely, $\langle \cdot \rangle = (\int_{A_f} \cdot \, \mathrm{d}A_f)/A_f$, where A_f indicates the plan area covered by the fluid at a given wall-normal height. Time-statistics reported in this work have been collected for different time integration intervals, T_{avg}, depending on the considered case. For each simulated case, T_{avg}, expressed in terms of external time units, δ/U_b, is reported in table 1. For the $k^+ = 90$ case, a significantly shorter integration time interval was used, in comparison with the other cases, to save on computational resources. For this case, the convergence of the statistics was checked by comparing the results for $T_{avg} = 140.9\delta/U_b$ and $T_{avg} = 94.7\delta/U_b$ and no significant differences were observed in the acquired statistics.

4. Results

Compared with a smooth-wall flow at matched Re_τ, a rough-wall flow exhibits increased momentum and scalar transfer which manifest themselves as a downward shift of the
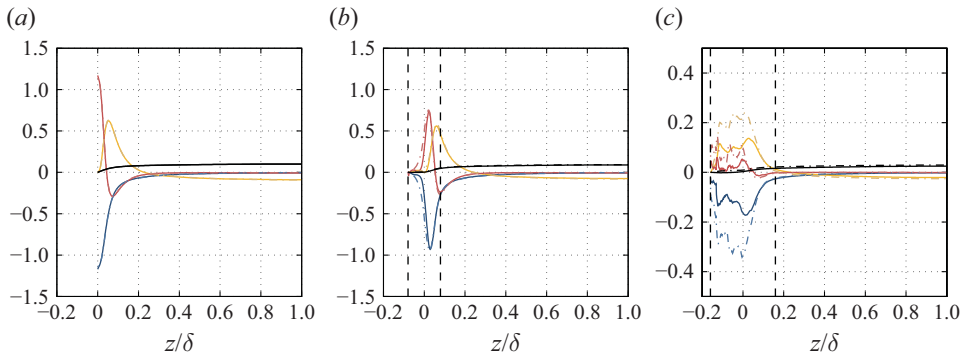
1006 R3-6

Figure 3. Mechanical- and scalar-energy budgets. (*a*) Smooth wall, $Re_\tau = 180$; (*b*) $k^+ = 15$, $Re_\tau = 180$; (*c*) $k^+ = 90$, $Re_\tau = 540$. ────, $-\varepsilon$; ─··─··─··, $-\varepsilon_\theta$; ────, $-T$; ─·─·─·, $-T_\theta$; ────, D; ─··─··─··, D_θ; ────, Π; ─··─··─··, Π_θ. The vertical black dashed lines in (*b*) and (*c*) indicate the boundaries of the roughness canopy.

logarithmic regions of the mean streamwise-velocity and scalar profiles (see, for instance, the review of Chung *et al.* 2021). This can be appreciated in figure 2, where the mean velocity and scalar profiles are shown for all the simulated cases. From an integral perspective, the roughness effect results in a decrease in the mean bulk velocity and scalar, U_b^+ and Θ_b^+, respectively. The latter, computed using (2.2*a*) and (2.2*b*), and the Reynolds-analogy factor (2.3) are reported in table 1. As expected, as the roughness Reynolds number, k^+, increases, so does the departure from the Reynolds analogy. This is shown by the faster decrease of U_b^+ compared with Θ_b^+ for increasing k^+. Correspondingly, the Reynolds-analogy factor decreases, from $RA = 1$ for the smooth-wall case, to $RA = 0.8$ for the $k^+ = 90$ case. As expected, while surface roughness promotes momentum and scalar exchange, the former is much favoured compared with the latter. Further, (2.2*a*) indicates that U_b^+ and Θ_b^+ represent, respectively, the total mechanical and scalar power realized by the flow for a specified mean pressure gradient and heat source. Hence, at fixed Re_τ, an increase in k^+ shows as a decrease in the total power that can be dissipated within the flow.

4.1. *Mechanical- and scalar-energy budgets*

The intrinsic average of the transport, viscous diffusion, dissipation and power-input terms of (2.1*a*) and (2.1*b*) are shown in figure 3. The definition of each term is reported in table 2. The power-input terms, Π and Π_θ, correspond to the mean streamwise-velocity and scalar profiles scaled by the Reynolds and Péclet numbers, respectively. Hence, the observations, made in reference to the mean profiles in figure 2, hold when comparing Π and Π_θ. Figure 3 further allows to relate the power input to the other terms in the budgets. For all the cases, towards the channel centre line, the viscous diffusion and the dissipation terms become negligible compared with the other terms, and $\Pi \approx T$ and $\Pi_\theta \approx T_\theta$. Closer to the wall, all terms in the budgets become relevant and each case needs to be addressed separately.

For the smooth-wall case, an almost perfect overlap is observed everywhere between the terms in the mechanical- and the scalar-energy equations. It should be noted that, at higher Reynolds numbers, such a perfect correspondence might be lost. As shown by Abe & Antonia (2017), at $Pr = 1$, and for sufficiently high Reynolds numbers, $U_b^+ = 2.54 \log(Re_\tau) + 2.41$ and $\Theta_b^+ = 2.18 \log(Re_\tau) + 4$. These two relations predict diverging

	Mechanical	Scalar
Transport	$T = \left\langle \overline{u_i^+ B_{,i}^+} \right\rangle$	$T_\theta = \left\langle \overline{u_i^+ \Gamma_{,i}^+} \right\rangle / Pr$
Diffusion	$D = \left\langle \overline{B}_{,ii}^+ \right\rangle$	$D_\theta = \left\langle \overline{\Gamma}_{,ii}^+ \right\rangle / (Pr^2)$
Dissipation	$\varepsilon = \left\langle \overline{\omega_i^+ \omega_i^+} \right\rangle$	$\varepsilon_\theta = \left\langle \overline{\theta_{,i}^+ \theta_{,i}^+} \right\rangle / (Pr^2)$
Power input	$\Pi = \frac{1}{Re_\tau} \delta_{1i} \left\langle \overline{u_i}^+ \right\rangle$	$\Pi_\theta = \frac{1}{Pe_\tau} \left\langle \overline{\theta}^+ \right\rangle$

Table 2. Definition of time- and space-averaged terms of the budget equations for $\overline{B}$ and $\overline{\Gamma}$.

U_b^+ and Θ_b^+ as the Reynolds number increases, with the scalar transfer becoming more effective than momentum transfer for sufficiently large Reynolds numbers (see below, figure 4a and the related discussion). Hence, differences can appear also in the budget terms shown in the figure.

For the $k^+ = 15$ case, figure 3(b) shows that roughness produces changes in the mechanical- and scalar-energy budget terms only well within the roughness canopy, leaving the distributions practically unaltered farther from the wall. Within the roughness canopy, the viscous diffusion is almost exclusively balanced by the dissipation term for both the mechanical and scalar budgets. Further, ε_θ and D_θ are amplified compared with ε and D. This scenario differs for the $k^+ = 90$ case in figure 3(c). Within the roughness canopy, the largest differences occur, whereas, away from the wall, the terms of the mechanical- and scalar-energy budgets tend to overlap, with the exception of T_θ and Π_θ which remain larger in magnitude than T and Π, respectively. Focusing on the mechanical-energy budget, the transport term T penetrates deep in the roughness sublayer, where it exceeds in magnitude the viscous diffusion D. Concurrently, the mechanical-energy dissipation exceeds, in magnitude, the joint contribution of T and D, thus realizing a slightly negative power input for $z \lesssim -0.045\delta$. The same cannot occur for the scalar power input Π_θ, for the scalar θ, and thus Π_θ, is bounded to vary in the interval [0, 1]. Consistently, within the roughness canopy, ε_θ retains a smaller magnitude compared with the joint contribution of T_θ and D_θ, therefore realizing a small, positive, Π_θ. Interestingly, the profiles of T_θ, D_θ and ε_θ are qualitatively similar in shape to the corresponding mechanical-energy budget terms, even though they are larger in magnitude.

4.2. *Mechanical and scalar dissipation*

The bulk mechanical and scalar dissipation, denoted respectively by $\mathcal{E}$ and $\mathcal{E}_\theta$, are defined as the volume average of the dissipation rates $\overline{\omega_i^+ \omega_i^+}$ and $\overline{\theta_{,i}^+ \theta_{,i}^+}$. Their relationship to the mean bulk velocity and scalar is given by (2.2a) and (2.2b). Figure 4(a) shows the computed values of U_b^+ and Θ_b^+ as functions of the friction Reynolds number. The plot shows also the logarithmic distributions expected for smooth-wall channel flow (Abe & Antonia 2016, 2017). The increase in momentum and scalar transfer introduced by the roughness causes the rough-wall data to lie below the smooth-wall asymptotes. The downward shift of U_b^+ and Θ_b^+ might rest upon different mean and turbulent flow contributions. This is verified by using the Reynolds decomposition to split $\mathcal{E}$ and $\mathcal{E}_\theta$ into their mean, $\mathcal{E}^m$, $\mathcal{E}_\theta^m$, and turbulent contributions, $\mathcal{E}^t$, $\mathcal{E}_\theta^t$, respectively.

The contributions to U_b^+ and Θ_b^+ of the mean and turbulent field are shown in figure 4(b) for the smooth- and rough-wall cases. Note that the smooth-wall data at $Re_\tau = 540$ are computed using the asymptotic relationships given by Abe & Antonia (2016, 2017). At $k^+ = 15$, the mean-flow contribution exceeds that due to the stochastic turbulent field.
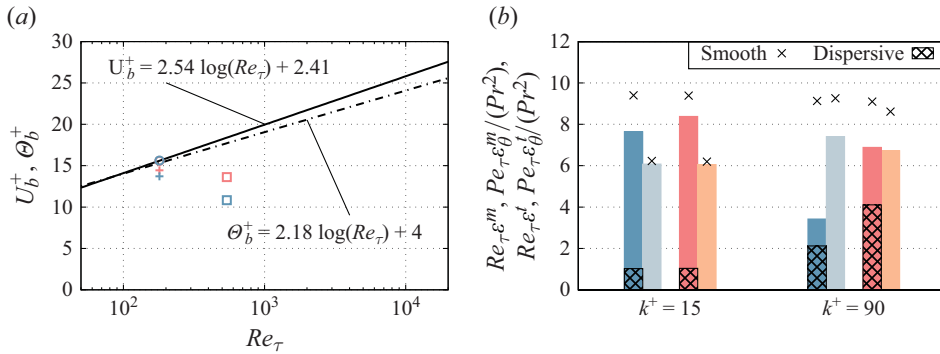
Figure 4. (*a*) Mean bulk velocity (blue) and scalar (red) as functions of the friction Reynolds number. Smooth wall, circle markers; rough wall $k^+ = 15$, cross markers; rough wall $k^+ = 90$, square markers. (*b*) Mean and turbulent contributions to the volume-averaged dissipation rates. ■, $Re_\tau \mathcal{E}^m$; ▨, $Re_\tau \mathcal{E}^t$; ■, $Pe_\tau \mathcal{E}_\theta^m / (Pr^2)$; ▨, $Pe_\tau \mathcal{E}_\theta^t / (Pr^2)$.

It is interesting to observe that $\mathcal{E}^t$, $\mathcal{E}_\theta^t$ attain similar values, which are also close to the smooth-wall data at the same Reynolds number. Conversely, $\mathcal{E}^m$ and $\mathcal{E}_\theta^m$ are reduced from the corresponding smooth-wall values, and $\mathcal{E}_\theta^m$ is approximately 10% larger than $\mathcal{E}^m$. Compared with the smooth-wall predictions at $Re_\tau = 540$, the rough-wall data at $k^+ = 90$ shows that $\mathcal{E}^m$ suffers the largest decrease, whereas $\mathcal{E}^t$, still being significantly lower than its corresponding smooth-wall counterpart, exceeds $\mathcal{E}^m$. On the other hand, $\mathcal{E}_\theta^m$ and $\mathcal{E}_\theta^t$ appear similar to each other.

Interestingly, figure 4(*b*) shows that, for both rough-wall cases, the largest contribution to the breaking of the Reynolds analogy appears to be caused by the mean-field: at $k^+ = 15$, $\mathcal{E}_\theta^m \approx 1.10 \mathcal{E}^m$ and $\mathcal{E}_\theta^t \approx \mathcal{E}^t$; at $k^+ = 90$, $\mathcal{E}_\theta^m \approx 1.96 \mathcal{E}^m$ and $\mathcal{E}_\theta^t \approx 0.93 \mathcal{E}^t$. Even though the limited amount of data are not sufficient to confirm this trend, it is instructive to further investigate the mean-flow contribution to U_b^+ and Θ_b^+. To do so, the time-averaged flow field is further decomposed in its time- and space-averaged parts and its dispersive (or wake) contribution $\overline{q} = \langle \overline{q} \rangle + \overline{q}''$, where $(\cdot)''$ indicates the dispersive fluctuation of $\overline{q}$. The contributions to $\mathcal{E}^m$ and $\mathcal{E}_\theta^m$ of, respectively, $\overline{\omega_i}''^+ \overline{\omega_i}''^+$ and $\overline{\theta_{,i}}''^+ \overline{\theta_{,i}}''^+$ are shown in figure 4(*b*) as hatched areas laid on top of the $\mathcal{E}^m$ and $\mathcal{E}_\theta^m$ boxes. At $k^+ = 15$, the dispersive components of the dissipation rates contribute little to $\mathcal{E}^m$ and $\mathcal{E}_\theta^m$ and their magnitude is very similar between the mechanical and scalar dissipation rates. As expected, this scenario changes significantly at $k^+ = 90$, as the dispersive contribution to $\mathcal{E}^m$ and $\mathcal{E}_\theta^m$ becomes the prominent one and $\overline{\theta_{,i}}''^+ \overline{\theta_{,i}}''^+$ significantly exceeds $\overline{\omega_i}''^+ \overline{\omega_i}''^+$.

Figure 5 compares the distributions of $\overline{\omega_i}''^+ \overline{\omega_i}''^+$ and $\overline{\theta_{,i}}''^+ \overline{\theta_{,i}}''^+$ within typical roughness patterns for the two rough-wall cases . High shear near roughness peaks leads to intense local heat and momentum transfer, where both fluxes exhibit a similar behaviour, as noted by Zhong, Hutchins & Chung (2023). Locally, the strong, positive, velocity and scalar gradients exceed significantly their spatial mean at the same wall-normal height, thus resulting in intense positive dispersive fluctuations $\overline{\omega_i}''^+$ and $\overline{\theta_{,i}}''^+$. Correspondingly, the dispersive dissipation fields, $\overline{\omega_i}''^+ \overline{\omega_i}''^+$ and $\overline{\theta_{,i}}''^+ \overline{\theta_{,i}}''^+$, attain their maxima. In figure 5, these regions are identified by isocontour lines for positive values of $\overline{\omega_y}''^+$ (figure 5a,c) and $\overline{\theta_{,z}}''^+$ (figure 5b,d). They grow attached to the windward side of roughness hills and develop, exposed to high shear, up to the hill's crest, where they eventually detach from
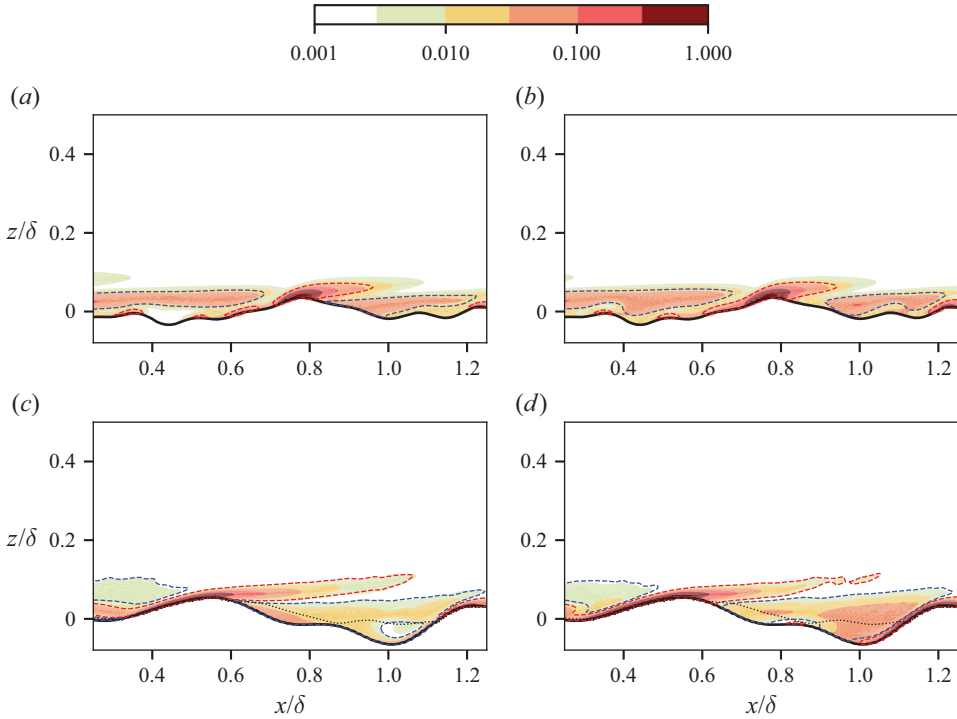
Figure 5. Dispersive dissipation rates for the $k^+ = 15$ (*a,b*) and $k^+ = 90$ (*c,d*) cases. Panels (*a,c*) show $\overline{\omega_i''^+ \omega_i''^+}$; (*b,d*) $\overline{\theta_{,i}''^+ \theta_{,i}''^+}$. Dashed lines represent lines of constant $\overline{\omega_y}''^+ = \pm 0.046$ (*a,c*) and $\overline{\theta_{,z}}''^+ = \pm 0.046$ (*b,d*). Blue and red colours indicate, respectively, negative and positive values. In panels (*c,d*), a black dotted line represents the isocontour line of zero mean streamwise velocity.

the roughness contour. Such regions will be named attached, exposed regions (AER) in the following. In AER, an apparent similarity is observed between $\overline{\omega_i''^+ \omega_i''^+}$ and $\overline{\theta_{,i}''^+ \theta_{,i}''^+}$.

Large roughness elements tend to shelter their downstream regions from the incoming flow, thereby generating pockets of slow-moving, recirculating flow, which entrain outer fluid towards the bottom of the roughness valleys (Forooghi, Stripf & Frohnapfel 2018). These regions are characterized by nearly uniform scalar distributions and smaller scalar gradients compared with their mean value at the same wall-normal height. This results in negative dispersive fluctuations of the scalar gradient, $\overline{\theta_{,i}}''^+$, which, in turn, increase the local dispersive dissipation rate $\overline{\theta_{,i}''^+ \theta_{,i}''^+}$. Hereafter, these regions will be referred to as well-mixed regions (WMR). The WMR are also characterized by negative dispersive fluctuations of the velocity gradient components, and hence of $\overline{\omega_i}''^+$, due to the slow-moving, possibly recirculating, flow. In figure 5, WMR are identified by isocontour lines for negative values of $\overline{\omega_y}''^+$ (figure 5*a,c*) and $\overline{\theta_{,z}}''^+$ (figure 5*b,d*). It can be seen how WMR extend throughout roughness valleys between large roughness elements. At $k^+ = 15$, WMR exhibit very similar distributions of dispersive dissipation rates. On the contrary, within these regions, significant differences are evident for the $k^+ = 90$ case, where $\overline{\theta_{,i}''^+ \theta_{,i}''^+}$ appears significantly larger than $\overline{\omega_i''^+ \omega_i''^+}$.

The spatial distributions of $\overline{\omega_i''^+ \omega_i''^+}$ and $\overline{\theta_{,i}''^+ \theta_{,i}''^+}$ represent an indication of how similarly the dissipation rates of $\overline{B}$ and $\overline{\Gamma}$ respond to the spatial changes imposed by the roughness topography. For instance, figures 5(*a*) and 5(*b*) clearly highlight differences in
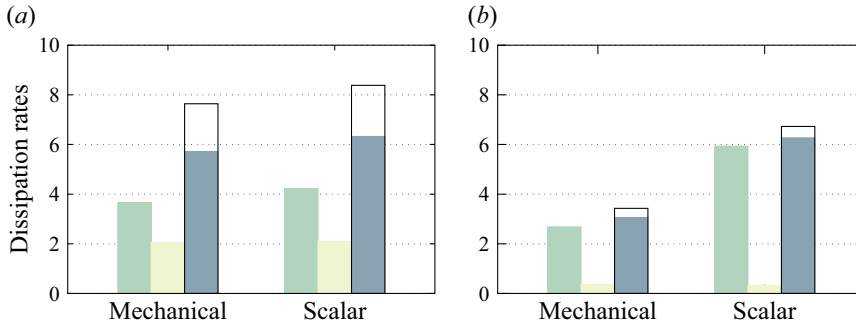
1006 R3-10

Figure 6. The AER and WMR contributions to $Re_\tau \mathcal{E}^m$ and $Pe_\tau \mathcal{E}^m_\theta/(Pr^2)$. (a) $k^+ = 15$; (b) $k^+ = 90$. ▮, AER; ▯, WMR; ▮, sum of AER and WMR contributions; a black solid outline indicates $Re_\tau \mathcal{E}^m$ and $Pe_\tau \mathcal{E}^m_\theta/(Pr^2)$.

the distributions of $\overline{\omega_i''^+ \omega_i''^+}$ and $\overline{\theta_{,i}''^+ \theta_{,i}''^+}$ within a WMR. Understanding the physical reasons for such dissimilarities requires further detailed analysis of local flow features. In the specific example of figures 5(a) and 5(b), the observed differences are likely related to the presence of separated, recirculating flow in the large roughness valley, in agreement with observations in the literature (for instance, see Spalart & Coleman 1997; MacDonald, Hutchins & Chung 2019) . The zero-mean-streamwise-velocity contour line in the figure emphasizes the back-flow at the bottom of the valley.

Although the visualization of $\overline{\omega_i''^+ \omega_i''^+}$ and $\overline{\theta_{,i}''^+ \theta_{,i}''^+}$ can provide a qualitative identification of flow regions where the dissipation rates behave dissimilarly, it does not provide an indication of the net contribution that such flow regions have on $\mathcal{E}^m$ and $\mathcal{E}^m_\theta$. However, this information can be obtained by assessing the mean dissipation rates, $\overline{\omega_i^+ \omega_i^+}$ and $\overline{\theta_{,i}^+ \theta_{,i}^+}$, over the identified flow regions. In particular, the relative contributions of AER and WMR to $\mathcal{E}^m$ and $\mathcal{E}^m_\theta$ is estimated by conditional integration of the mean dissipation rates.

This is achieved by integrating $\overline{\omega_i^+ \omega_i^+}$ and $\overline{\theta_{,i}^+ \theta_{,i}^+}$ over AER and WMR. The former were identified as the regions over which $\overline{\theta}_{,z}''^+ > 0.046$, whereas for the latter, the condition $\overline{\theta}_{,z}''^+ < -0.046$ was used. This particular choice was made based on the visual inspection of the flow and upon noting that these two conditions correlate well with the presence of AER and WMR, as visualized in figure 5, throughout the roughness canopy.

Figure 6 shows the result of the conditional integration of the dissipation rates, normalized by the empty channel volume. For both cases, the largest contribution to $\mathcal{E}^m$ and $\mathcal{E}^m_\theta$ is introduced by AER, whereas the contribution of WMR, despite being significant at $k^+ = 15$, becomes marginal at $k^+ = 90$. Interestingly, the contribution of WMR is very similar for the mechanical and scalar dissipation rates at both roughness Reynolds numbers. Namely, the dissimilarity between $\mathcal{E}^m$ and $\mathcal{E}^m_\theta$ can be attributed to the differences displayed by the dissipation rates in AER alone. Note that the joint contribution of AER and WMR accounts for a large part of $\mathcal{E}^m$ and $\mathcal{E}^m_\theta$, especially at $k^+ = 90$, where it represents more than 90% of $\mathcal{E}^m$ and $\mathcal{E}^m_\theta$. The residual represents the contribution of the mean-flow dissipation rates that takes place in the core of the channel.

5. Conclusions

The present work explored a novel perspective for the assessment of the Reynolds analogy in turbulent, forced convection. In particular, it is shown that B (the total mechanical

energy, sum of the kinetic energy and pressure work) and Γ (one-half of the squared scalar field) share a similar structure in their time-averaged governing equations. For fully developed channel-flow configurations, the integral balance of total mechanical and scalar energy allows expressing the mean bulk velocity U_b^+ and scalar Θ_b^+ in terms of the volume averages of the dissipation fields $\overline{\omega_i^+ \omega_i^+}$ and $\overline{\theta_{,i}^+ \theta_{,i}^+}$, respectively. In turn, the Reynolds-analogy factor (the ratio between the total mechanical and scalar energy realized by the flow, i.e. U_b^+/Θ_b^+) can be related to the dissipation fields.

This energetic perspective on the Reynolds-analogy problem enables the identification of flow regions where departures from the analogy occur and provides a means for quantifying their net effect on the momentum and scalar transfer. This approach was showcased on fully developed turbulent channel flow over homogeneous surface roughness, a well-known instance of the failure of the Reynolds analogy. The study presented DNS results of two rough-wall turbulent channel flows at $k^+ = 15$ and $k^+ = 90$. In addition, a smooth-wall channel flow at $Re_\tau = 180$ was also considered. For all the cases, a unit Prandtl number was considered.

The present data show that similarity exists between the time- and space-averaged wall-normal distributions of the mechanical and scalar budget-equation terms. For the smooth-wall case, each term overlaps in both equations. For the rough-wall cases, roughness amplifies significantly $\overline{\Gamma}$ budget-equation terms while maintaining similar shapes of the corresponding terms in the $\overline{B}$ budget equation.

An increase in k^+ determines a decrease in the total power exerted by the flow; equivalently, the total energy dissipated within the flow decreases as the roughness Reynolds number increases. For the present data, roughness affects more significantly the volume-averaged mean dissipation rates, $\mathcal{E}^m$ and $\mathcal{E}_\theta^m$, compared with the turbulent contributions $\mathcal{E}^t$ and $\mathcal{E}_\theta^t$. While at $k^+ = 15$ the latter are practically unchanged, compared with their smooth-wall equivalent at matched Re_τ, at $k^+ = 90$, the relative change, compared with the smooth-wall reference, of $\mathcal{E}^m$, $\mathcal{E}_\theta^m$ exceeds that of $\mathcal{E}^t$, $\mathcal{E}_\theta^t$. Further, at both roughness Reynolds numbers, the largest departure from Reynolds analogy is observed for the mean-flow dissipation contributions, whereas $\mathcal{E}^t$ and $\mathcal{E}_\theta^t$ remain similar. It is noted that further data are necessary to explore higher Reynolds number scenarios, whereby the turbulent contributions to the dissipation rates possibly start to play a dominant role in shaping the asymptotic behaviours of U_b^+ and Θ_b^+.

The analysis of the mean dissipation rates reveals the flow regions that contribute the most to the mean scalar and momentum transfer within the roughness sublayer. These are AER, which develop on the windward side of roughness hills, and WMR, which occur within the valleys of the roughness topography. In both cases, AER contribute most significantly to $\mathcal{E}^m$ and $\mathcal{E}_\theta^m$, while the net contribution of WMR becomes negligible at $k^+ = 90$. Interestingly, the WMR contribution is nearly identical for both mechanical and scalar dissipation rates for the two investigated roughness Reynolds numbers. This indicates that the observed dissimilarity between $\mathcal{E}^m$ and $\mathcal{E}_\theta^m$ arises primarily from differences in the dissipation rates within AER alone.

This analysis highlights the role that AER and WMR have, in different flow regimes, on momentum and scalar transfer over rough walls, in agreement with observations in the literature (Zhong *et al.* 2023). Future studies should expand upon the present findings by examining a broader range of roughness Reynolds numbers and roughness topographies; in this context, the presented energetic perspective can be valuable for exploring asymptotic scalar transfer laws in the fully rough regime.

REFERENCES

ABE, H. & ANTONIA, R.A. 2016 Relationship between the energy dissipation function and the skin friction law in a turbulent channel flow. *J. Fluid Mech.* **798**, 140–164.

ABE, H. & ANTONIA, R.A. 2017 Relationship between the heat transfer law and the scalar dissipation function in a turbulent channel flow. *J. Fluid Mech.* **830**, 300–325.

ABE, H., ANTONIA, R.A. & KAWAMURA, H. 2009 Correlation between small-scale velocity and scalar fluctuations in a turbulent channel flow. *J. Fluid Mech.* **627**, 1–32.

ANTONIA, R.A., ABE, H. & KAWAMURA, H. 2009 Analogy between velocity and scalar fields in a turbulent channel flow. *J. Fluid Mech.* **628**, 241–268.

BRADSHAW, P. & KOH, Y.M. 1981 A note on Poisson's equation for pressure in a turbulent flow. *Phys. Fluids* **24** (4), 777–777.

CHUNG, D., HUTCHINS, N., SCHULTZ, M.P. & FLACK, K.A. 2021 Predicting the drag of rough surfaces. *Annu. Rev. Fluid Mech.* **53** (1), 439–471.

CORRSIN, S. 1952 Heat transfer in isotropic turbulence. *J. Appl. Phys.* **23** (1), 113–118.

FISHER, P.F., LOTTES, J.W. & KERKEMEIER, S.G. 2019 *NEK5000 Version 19.0*. Argonne National Laboratory.

FOROOGHI, P., STRIPF, M. & FROHNAPFEL, B. 2018 A systematic study of turbulent heat transfer over rough walls. *Intl J. Heat Transfer* **127**, 1157–1168.

HANTSIS, Z. & PIOMELLI, U. 2022 Effects of roughness on the turbulent Prandtl number, timescale ratio, and dissipation of a passive scalar. *Phys. Rev. Fluids* **7** (12), 124601.

HANTSIS, Z. & PIOMELLI, U. 2024 Numerical simulations of scalar transport on rough surfaces. *Fluids* **9** (7), 159.

HASEGAWA, Y. & KASAGI, N. 2011 Dissimilar control of momentum and heat transfer in a fully developed turbulent channel flow. *J. Fluid Mech.* **683**, 57–93.

KASAGI, N., TOMITA, Y. & KURODA, A. 1992 Direct numerical simulation of passive scalar field in a turbulent channel flow. *J. Heat Transfer* **114** (3), 598–606.

KIM, J. & MOIN, P. 1989 Transport of passive scalars in a turbulent channel flow. In *Turbulent Shear Flows* (ed. J.C. André, J. Cousteix, F. Durst, B.E. Launder, F.W. Schmidt & J.H. Whitelaw), vol. 6, pp. 85–96, Springer.

LAADHARI, F. 2007 Reynolds number effect on the dissipation function in wall-bounded flows. *Phys. Fluids* **19** (3), 038101.

LEONARDI, S., ORLANDI, P., DJENIDI, L. & ANTONIA, R.A. 2015 Heat transfer in a turbulent channel flow with square bars or circular rods on one wall. *J. Fluid Mech.* **776**, 512–530.

MACDONALD, M., HUTCHINS, N. & CHUNG, D. 2019 Roughness effects in turbulent forced convection. *J. Fluid Mech.* **861**, 138–162.

PATERA, A.T. 1984 A spectral element method for fluid dynamics: laminar flow in a channel expansion. *J. Comput Phys.* **54** (3), 468–488.

PEETERS, J.W.R. & SANDHAM, N.D. 2019 Turbulent heat transfer in channels with irregular roughness. *Intl J. Heat Transfer* **138**, 454–467.

PIROZZOLI, S., BERNARDINI, M. & ORLANDI, P. 2016 Passive scalars in turbulent channel flow at high Reynolds number. *J. Fluid Mech.* **788**, 614–639.

REYNOLDS, O. 1874 On the extent and action of the heating surface of steam boilers. *Proc. Lit. Phil. Soc. Manchester* **14**, 7–12.

SPALART, P.R. & COLEMAN, G.N. 1997 Numerical study of a separation bubble with heat transfer. *Eur. J. Mech. (B/Fluids)* **16** (2), 169–189.

THAKKAR, M. 2017 Investigation of turbulent flow over irregular rough surfaces using direct numerical simulations. PhD thesis, University of Southampton, UK.

THAKKAR, M., BUSSE, A. & SANDHAM, N. 2017 Surface correlations of hydrodynamic drag for transitionally rough engineering surfaces. *J. Turbul.* **18** (2), 138–169.

THAKKAR, M., BUSSE, A. & SANDHAM, N.D. 2018 Direct numerical simulation of turbulent channel flow over a surrogate for Nikuradse-type roughness. *J. Fluid Mech.* **837**, R1.

WEI, T. 2018 Integral properties of turbulent-kinetic-energy production and dissipation in turbulent wall-bounded flows. *J. Fluid Mech.* **854**, 449–473.

WU, J.Z., ZHOU, Y. & FAN, M. 1999 A note on kinetic energy, dissipation and enstrophy. *Phys. Fluids* **11** (2), 503–505.

ZHONG, K., HUTCHINS, N. & CHUNG, D. 2023 Heat-transfer scaling at moderate Prandtl numbers in the fully rough regime. *J. Fluid Mech.* **959**, A8.